Monthly Notices
of the
ROYAL ASTRONOMICAL SOCIETY

MNRAS **507,** 963–970 (2021)
Advance Access publication 2021 August 3

https://doi.org/10.1093/mnras/stab2117

Discovery of a possible splashback feature in the intracluster light of MACS J1149.5+2223

Anthony H. Gonzalez [1]★ Tyler George,[1] Thomas Connor,[2,3]† Alis Deason [4,5] Megan Donahue,[6] Mireia Montes [7] Ann I. Zabludoff [8] and Dennis Zaritsky [8]

[1]*Department of Astronomy, University of Florida, Gainesville, FL 32611, USA*
[2]*Jet Propulsion Laboratory, California Institute of Technology, 4800 Oak Grove Drive, Pasadena, CA 91109, USA*
[3]*The Observatories of the Carnegie Institution for Science, 813 Santa Barbara St, Pasadena, CA 91101, USA*
[4]*Institute for Computational Cosmology, Department of Physics, University of Durham, South Road, Durham DH1 3LE, UK*
[5]*Centre for Extragalactic Astronomy, Department of Physics, University of Durham, South Road, Durham DH1 3LE, UK*
[6]*Department of Physics and Astronomy, Michigan State University, East Lansing, MI 48824, USA*
[7]*Space Telescope Science Institute, Baltimore, MD 21218, USA*
[8]*Department of Astronomy & Steward Observatory, University of Arizona, Tucson, AZ 85721, USA*

Accepted 2021 July 15. Received 2021 June 23; in original form 2021 April 18

ABSTRACT

We present an analysis of the intracluster light (ICL) in the Frontier Field Cluster MACS J1149.5+2223 ($z = 0.544$), which combines new and archival *Hubble* WFC3/IR imaging to provide continuous radial coverage out to 2.8 Mpc from the brightest cluster galaxy (BCG). Employing careful treatment of potential systematic biases and using data at the largest radii to determine the background sky level, we reconstruct the surface brightness profile out to a radius of 2 Mpc. This radius is the largest to which the ICL has been measured for an individual cluster. Within this radius, we measure a total luminosity of 1.5×10^{13} $L_{\odot}$ for the BCG plus ICL. From the profile and its logarithmic slope, we identify the transition from the BCG to ICL at $r \sim$ 70 kpc. Remarkably, we also detect an apparent inflection in the profile centred in the 1.2–1.7 Mpc (0.37–0.52 r_{200m}) radial bin, a signature of an infall caustic in the stellar distribution. Based upon the shape and strength of the feature, we interpret it as potentially being at the splashback radius, although the radius is smaller than theoretical predictions. If this is the splashback radius, then it is the first such detection in the ICL and the first detection of the splashback radius for an individual cluster. Similar analyses should be possible with the other Frontier Field clusters, and eventually with clusters observed by the *Euclid* and *Roman* missions.

Key words: galaxies: clusters: general – galaxies: evolution.

1 INTRODUCTION

It has been seven decades since Zwicky (1951) first noted extended, diffuse emission in the Coma cluster. Because this diffuse emission is typically centred on the brightest cluster galaxy (BCG; e.g. Schombert 1988; Gonzalez, Zabludoff & Zaritsky 2005), in early literature this component was often referred to as a cD envelope (e.g. Oemler 1973), but is now most commonly referred to as intracluster light (ICL). The stars that comprise the ICL are by definition unbound from individual galaxies, and instead orbit in the gravitational potential well of the cluster. ICL studies have gained in prominence in recent years, driven primarily by the realization that this component encodes key information about the global cluster properties and the evolution of galaxy clusters (e.g. Montes 2019).

Specifically, there are three dominant questions that have motivated research on the ICL. The first is how much mass the ICL contributes to the baryon budget in clusters. A number of authors find that the ICL contains a non-negligible fraction of the total stellar mass in cluster cores (e.g. Gonzalez, Zaritsky & Zabludoff 2007; Gonzalez et al. 2013; Laganá et al. 2013; Furnell et al. 2021), and thus cannot be ignored in a census of cluster baryons. However, until the recent work of Sampaio-Santos et al. (2020), even the studies with the greatest radial coverage (Zibetti et al. 2005; Zhang et al. 2019) lacked the combination of radial range and surface brightness sensitivity to reach a point where the measured total stellar mass in the ICL converges, and only one published result for an individual cluster reached a projected radius of 1 Mpc (Abell 1413; Schombert 1986, 1988).

The second open question is the origin and assembly history of the ICL, which is central to understanding the global evolution of the cluster galaxy population. Recent observational studies find significant late-time build-up of the ICL (DeMaio et al. 2020; Furnell et al. 2021) and inside-out growth (DeMaio et al. 2020). Whether the bulk of the ICL arises from tidal disruption of low-mass dwarf galaxies (Giallongo et al. 2014; Annunziatella et al. 2016) or tidal stripping of the outskirts of more massive galaxies (Montes & Trujillo 2014, 2018; DeMaio et al. 2015, 2018) remains an unsettled question,

★ E-mail: anthonyhg@ufl.edu
† NPP Fellow.

impeding interpretation of integrated cluster galaxy properties such as the luminosity function.

The third question centres on how well the ICL traces the gravitational potential of the host cluster. Montes & Trujillo (2019) demonstrated for the *Hubble* Frontier Field (HFF) clusters that the ICL is an accurate luminous tracer of the lensing mass distribution within the central 140 kpc, and hence argued that the ICL traces the dark matter significantly better than X-ray emission. Subsequent investigation by Alonso Asensio et al. (2020) using the C-EAGLE simulations indicates that the intrinsic correlation is even tighter than observed by Montes & Trujillo (2019). As such, the ICL potentially provides an efficient means of mapping out cluster mass distributions in future surveys with the *Euclid* and *Roman* missions. Sampaio-Santos et al. (2021) have also recently argued that the total ICL stellar mass scales with cluster mass, providing a low-scatter proxy for total cluster mass and further enhancing the potential utility of ICL for future cluster studies.

Beyond the questions above, there is another area in which the ICL may be of particular use: defining the halo boundary and connecting observations with simulations. When matter falls into a halo, the apocentre of its initial orbit constitutes an observable physical radius (Gunn & Gott 1972; Fillmore & Goldreich 1984; Bertschinger 1985). Diemer & Kravtsov (2014) pointed out that this 'splashback' radius is often characterized by a sharp break in the density profile. The location of this feature can be directly predicted by simulations; at a given redshift the radial location of this feature is determined by cluster mass and accretion rate (Adhikari, Dalal & Chamberlain 2014; Diemer & Kravtsov 2014; More, Diemer & Kravtsov 2015; Umetsu & Diemer 2017; Diemer 2020; Xhakaj et al. 2020; O'Neil et al. 2021).

Recent observational programs have detected the splashback radius for ensembles of stacked clusters via galaxy surface density profiles (More et al. 2016; Shin et al. 2019; Zürcher & More 2019; Adhikari et al. 2020; Murata et al. 2020; Bianconi et al. 2021) or weak gravitational lensing (Contigiani, Hoekstra & Bahé 2019), confirming the existence of this feature. Of direct relevance to this work, Deason et al. (2021) used the C-EAGLE simulations to demonstrate that this signature is expected in the ICL. Given the results of Sampaio-Santos et al. (2021), if the total ICL stellar mass and splashback radius can be measured, then in principle one can determine both accretion histories and cluster masses. Moreover, measurements of the splashback radii for individual clusters would facilitate environmental studies of the cluster galaxy population, particularly enabling a clear identification of currently infalling galaxies beyond the splashback radius.

Here, we focus on the cluster MACS J1149.5+2223 ($z = 0.544$; Ebeling, Edge & Henry 2001; Ebeling et al. 2007). This cluster was part of the Cluster Lensing and Supernova survey with *Hubble* (CLASH Postman et al. 2012) and is one of the six HFFs (Lotz et al. 2017). In addition to being an extremely massive cluster ($M_{200m} = 3.4 \pm 0.7 \times 10^{15}$ $M_\odot$; Umetsu et al. 2014), it is known to be a complex ongoing merger. Golovich et al. (2016) find evidence for three distinct merging components, including a major merger of roughly equal mass components plus accretion of a third, lower mass subcluster. These properties and the extensive existing data make MACS J1149.5+2223 a unique system for a detailed investigation of the distribution and properties of the ICL, and these data have been previously used by multiple groups to investigate the ICL in the cluster core (Morishita et al. 2017; Montes & Trujillo 2018). In this program, we significantly extend the radial regime over which the ICL can be studied.

Using a combination of new and archival *HST* observations, we trace the surface brightness profile of the ICL out to 2 Mpc. We quantify the total luminosity contained within this diffuse component and demonstrate the feasibility of probing the ICL to large radii with upcoming space-based survey missions. We also investigate whether we can detect caustic signatures – edges in the matter phase space distribution that are detectable as edges in the density distribution – in the radial profile, as predicted by Deason et al. (2021). We save consideration of the two-dimensional distribution of the ICL, and of the origin of the ICL, for future companion papers. Throughout this paper, r_{200m} is defined relative to the mean density of the Universe, and we use the cosmological parameters of the Planck Collaboration XIII (2016). Specifically, $H_0 = 67.7$ km s^{-1} Mpc^{-1}, $\Omega_m = 0.307$, and $\Omega_\Lambda = 0.693$.

2 HST DATA

The data used in this analysis consist of a combination of all archival *F*105*W* and *F*160*W* data for MACS J1149.5+2223 taken prior to 2019, including associated parallel field data and new observations from program *HST*-GO-15308 (PI: Gonzalez) in these same filters. The choice of filters is based upon similar criteria to those used for DeMaio et al. (2018), as explained below. We focus our attention on WFC3/IR data due to its sensitivity to emission from relatively old stellar populations, for which the spectral energy distributions peak in the near-infrared. The predominant source of archival data for this program is the HFF program, which observed MACS J1149.5+2223 in *F*105*W*, *F*125*W*, *F*140*W*, and *F*160*W*. The *F*105*W* and *F*160*W* filters together provide the longest wavelength lever arm, which is beneficial for identifying colour gradients in the ICL. A consideration with *F*105*W* data is that there exists a time-variable excess Earth glow in this passband due to the Helium 1.038 μm emission line (see Instrument Science Report WFC3 2014-03). To minimize the impact of this Helium line, we acquired *F*105*W* observations during the middle of each orbit when the Earth glow would be lowest.

The program IDs, dates, number of exposures, total exposure times, and filters for all archival data used in this analysis are listed in Table 1. The Table also includes an indication of whether the pointing was centred on the cluster core (Core), a parallel field (Parallel), or is a bridging field (Bridge) .

The new observations consist of three bridging fields designed to uniformly span the gap between the cluster core and parallel fields. The geometry of these fields is schematically shown in Fig. 1. We refer to these fields as Bridge 1, Bridge 2, and Bridge 3 in Table 1, where we present the exposure information. The exposure times for the bridge fields correspond to 1 orbit per filter per pointing. These modest observations are sufficient because we are limited in this analysis by systematic rather than statistical uncertainties at large radii.

3 METHODS

3.1 Data processing

We reprocess the data starting with the calibrated individual exposures (`flt` images) in a similar fashion to DeMaio et al. (2018). All images are processed with the standard ASTRODRIZZLE routines (Gonzaga, Fruchter & Mack 2012) and drizzled on to a common reference frame with a pixel scale of 0.1 arcsec. One important difference relative to the standard reduction provided by STScI is that we do not subtract the sky from the individual images to avoid unintentional subtraction of the ICL. As in DeMaio et al. (2018), we

Table 1. Data sets included in this analysis.

PID	Filter	Dates	# of images	Exp. time (ks)
		Core		
12068	*F*105*W*	30 Jan 2011–27 Feb 2011	5	2.8
	*F*160*W*	04 Dec 2010–09 Mar 2011	24	13.5
13504	*F*105*W*	21 Nov 2014–05 Jan 2015	48	67.3
	*F*160*W*	02 Nov 2013–05 Jan 2015	48	66.1
13790	*F*105*W*	20 2015–13 Jul 2015	16	6.3
	*F*160*W*	29 Nov 2014–21 Jul 2015	63	24.0
14199	*F*105*W*	12 Feb 2016–14 Feb 2016	8	6.8
	*F*160*W*	30 Oct 2015–30 Oct 2016	71	29.6
14208	*F*105*W*	16 May 2016	3	1.2
	*F*160*W*	16 May 2016	4	2.3
14528	*F*160*W*	14 Jul 2016–20 Jul 2016	9	3.6
14872	*F*160*W*	05 Dec 2016	3	1.2
		Parallel		
13504	*F*105*W*	19 Apr 2015–09 May 2015	48	64.4
	*F*160*W*	14 Apr 2014–09 May 2015	48	66.5
		Bridge 1		
15308	*F*105*W*	25 May 2018	4	2.4
	*F*160*W*	25 May 2018	4	2.4
		Bridge 2		
15308	*F*105*W*	25 Apr 2018	4	2.4
	*F*160*W*	25 Apr 2018	4	2.4
		Bridge 3		
15308	*F*105*W*	26 May 2018	4	2.4
	*F*160*W*	26 May 2018	4	2.4

also use data obtained at a similar epoch to each observation to apply a flat-fielding correction to each image.

The current processing does diverge from that of DeMaio et al. (2018) in several significant ways. First, in DeMaio et al. (2018) a planar gradient was subtracted from each exposure. We omit this step in the current analysis to fully preserve the ICL signal at large radii. Second, we mask pixels that are potentially contaminated by residual charge from previous observations (persistence). Third, we generate epoch-specific flat-fields specifically for this analysis. Finally, there are some minor changes in the implementation of masking more generally to ensure consistency between overlapping images. Details of the persistence masking, flat-field correction, and masking implementation are described below.

3.1.1 *Persistence*

Bright sources observed by the WFC3/IR detector leave residual charge after the observation which can result in an observed excess in the counts at that location in subsequent images (Smith et al. 2008). The level of this persistence is a function of time after the observation and the brightness of the previous source. Persistence maps for all WFC3/IR observations are provided by the WFC Persistence Project through the Mikulski Archive for Space Telescopes (MAST).[1] These maps include the impact of images taken up to 16 h prior to the observations. It was emphasized by Borlaff et al. (2019) that images taken even further prior to an observation can still have a noticeable impact at the lowest surface brightness levels, and for their analysis of the *Hubble* Ultra Deep Field those authors generated persistence maps using data from the previous 96 h. However, for the current analysis, in which we are focusing upon the radially averaged profile, the default persistence images are sufficient.

In the pipeline, for individual exposures we mask all pixels for which the persistent charge exceeds a level equivalent to $\mu = 33$ mag arcsec^{-1}. This is over a magnitude below the faintest level to which we trace the *F*105*W* surface brightness profile, and the impact of persistence is further diluted by the radial binning. We also reject 18 *F*160*W* images of the cluster core (4 per cent of the total data, 3 from program 13790 and 15 from program 14199) that are severely compromised by persistence across much of the field.

3.1.2 *Flat-fields*

As has been pointed out in several papers (Borlaff et al. 2019; DeMaio et al. 2020, and references therein), the sensitivity of the WFC3/IR detector has a long-term temporal component that for ICL analyses can be a dominant systematic uncertainty if data are processed using only the default WFC3/IR flats. For this analysis, we therefore generate flat-field corrections (hereafter Δ flats) for a series of epochs corresponding to the MACS J1149.5+2223 observation epochs.

We start with all WFC3/IR science observations in the *F*105*W* and *F*160*W* filters from the period of 2010 January through 2019 December that were publicly available in the *HST* archive as of 2020 March. From this sample, we next exclude observations that (i) have short exposure times of <400 s in *F*105*W* or <300 s in *F*160*W*, or (ii) target regions for which extended structures would be expected to compromise the flat-field (including extended low-redshift galaxies, galaxy clusters, regions with significant nebulosity, and dense stellar fields). All remaining images are then visually inspected by a member of our team (TG) to remove any additional images that are otherwise unsuitable for inclusion when generating a flat. This visual inspection removed approximately 2 per cent of the images.

For this restricted set of observations, we then define a set of fiducial dates and use an initial window of $\pm$6 months to generate lists of images from which to construct Δ flats. We further require a minimum of 250 (200) input images in *F*160*W* (*F*105*W*) for each Δ flat, and therefore widen time windows as necessary to reach this threshold. This is generally more of an issue for *F*105*W*, for which the final windows range from $\pm$270 to $\pm$420 d. The list of fiducial dates, window widths, and number of input images are given in Table 2.

To generate the Δ flats, we start with `flt` files, for which the original default flat-field has already been applied. For each image, we generate object masks using the PYRAF command `objmasks` with a 3 $\times$ 3 convolution kernel (Science Software Branch at STScI 2012), masking all 2σ detections with an area of >50 pixels and growing the mask around each object. We then also apply the persistence masks from Section 3.1.1. Using these masks, we median scale the `flt` images, median combine them with 5σ outlier rejection, and normalize to create output Δ flats. In addition to correcting subtle large-scale trends, the Δ flats minimize localized 'holes' in the response that have developed over time.

3.1.3 *Masking*

The standard ASTRODRIZZLE reduction yields a single combined image for each epoch and filter, as well as associated context (`ctx`) and weight (`wht`) images. We first use the `ctx` image, which contains

[1] See https://archive.stsci.edu/prepds/persist.

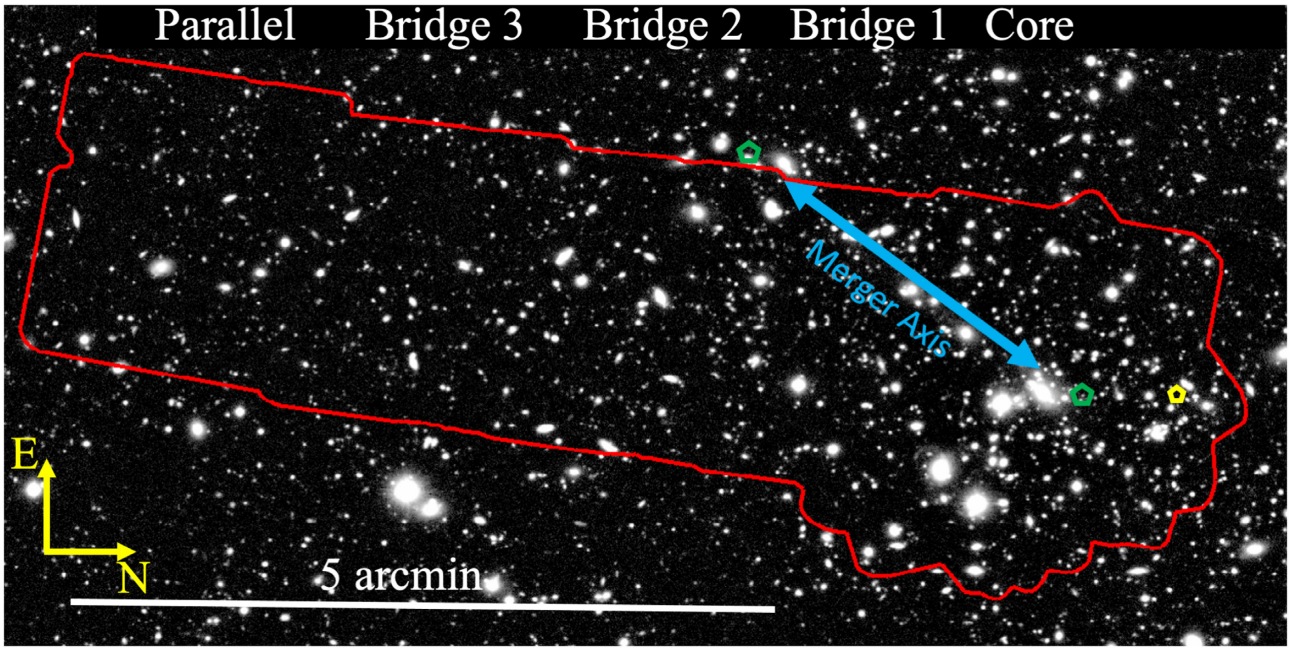

Figure 1. Shown here is the coverage of the *HST* WFC3/IR *F*105*W* data (red contours) overlaid on a Subaru *z*-band image from CLASH (Postman et al. 2012), illustrating the geometry of the bridge fields relative to the core and parallel fields. North is to the right, and east is up. The core and parallel fields are primarily from the CLASH (Postman et al. 2012) and HFF (Lotz et al. 2017) surveys. Each bridge field overlaps by approximately 20 per cent with adjacent fields. Together these fields enable continuous radial coverage and correction for sky level offsets between the core and parallel observations. The blue arrow illustrates the axis of the main ongoing cluster merger (Golovich et al. 2016), which is oriented approximately 30 deg from the long axis of our *HST* imaging.The two green and pentagons denote the centroids from Golovich et al. (2016) for these two subclusters. We denote the location of the third subcluster found in that study, which contributes only 4 per cent of the total mass, with a yellow pentagon. For scale, 5 arcmin corresponds to 1.97 Mpc at the cluster redshift.

Table 2. Definition of epochs for construction of Δ flats.

Date	Half-width (d)	# images
	*F*105*W*	
2011 Feb 14	330	208
2014 Dec 14	270	226
2015 Apr 30	270	287
2015 Jul 08	270	291
2016 Mar 27	360	251
2018 May 10	420	203
	*F*160*W*	
2011 Jan 20	180	984
2013 Nov 02	180	308
2014 Apr 14	270	300
2014 Dec 29	225	247
2015 Apr 15	180	305
2015 Sep 30	180	403
2016 Apr 15	180	252
2016 Nov 15	300	258
2018 May 10	180	283

information on which input images contribute to each output science image, to create a mask for each image. We then multiply this mask by the persistence mask. All images are then transformed to a common reference frame using `scamp` and `swarp` (Bertin 2010a, b). Next, all images in a given filter and at a given location (i.e. core, parallel, or each bridge field) are coadded and SExtractor (Bertin & Arnouts 1996) is used to construct an object catalogue for each location.[2] These catalogues are used as input to generate elliptical masks which excludes pixels within two Kron radii for all objects in the field, including cluster members, except for the BCG which is left unmasked. Additionally, we use a manually generated region file to mask galaxies near the core of the BCG that are missed by SExtractor. These galaxies, which are identified via visual inspection, are masked with large circular apertures.

Once these masks are generated for each location, they are combined to make a composite mask for the full area in each filter. This composite mask is a union of the individual masks – any pixel excluded in any of them is excluded in the composite. Finally, the *F*105*W* and *F*160*W* composite masks are combined to make a final joint mask excluding all pixels masked at either wavelength.

3.2 Sky normalization

At this stage we are ready to correct for relative offsets in the sky level between observations taken at different epochs due to variations in zodiacal light, Earth-shine, and atmospheric He I emission (Brammer et al. 2014; Pirzkal 2014). We define a single parallel exposure to be the reference frame, to which we will normalize the sky level for all other exposures. The procedure is straightforward. For each image overlapping with the reference frame, which includes all parallel images and Bridge3, we compute the median sky level (f) in the unmasked overlap region between that image and the reference

[2]We set the SExtractor detection parameters with a minimum area of 5 pixels and a 2σ detection threshold.

image. Each image i is then normalized via

$$f_i' = f_i + \text{median}[f_{\text{ref}}(\text{overlap})] - \text{median}[f_i(\text{overlap})]. \quad (1)$$

Next, we use the same procedure to step through the bridge fields, starting with normalizing the Bridge 2 images to match the level of Bridge 3 in the overlap region between the two. We then normalize a single core image to Bridge 1, and use this as a reference frame within the core region to which all other core images are normalized. The maximum normalization corrections to the core images to match the parallel reference image were ∼7–8 × 10^{-3} counts s^{-1} for both filters.

The above procedure results in a robust relative sky calibration from the core to the parallel fields. We note that the results are robust to which parallel image is chosen as the reference image. At this point we only lack an absolute calibration of the sky level. The approach that we take in Section 4.1 is to use data at the largest radii covered by the parallel imaging to define a zero sky level, and verify that the results are robust to the exact choice of annular sky aperture.

4 ANALYSIS AND RESULTS

4.1 Radial profiles

We compute median radial surface brightness profiles in circular apertures with logarithmic bins of width dlog $r = 0.15$ starting with an inner radius of 1 arcsec (∼6.6 kpc). Use of the median helps to minimize bias arising from local substructures, as pointed out by Mansfield, Kravtsov & Diemer (2017) and Deason et al. (2021).[3] While the cluster mass distribution is highly elongated ($b/a = 0.37$, oriented 38.5° west of north; Umetsu et al. 2018), we intentionally choose to use a circular aperture because it is not practical – either in this case or in most other observations – to appropriately model the ellipticity as a function of radius. Hence, a simple circular aperture provides the most transparent means of comparing with simulations. These profiles are computed individually for each epoch, filter, and field, resulting in a total of 44 separate profiles. We compute the composite profile by calculating the mean and standard deviation for all measurements within each radial bin. The outermost bin in our radial profile is centred at 1.96 Mpc and has an outer radius of 2.31 Mpc. As noted above, one remaining uncertainty is that we have a relative calibration of the sky level in each image but not an absolute calibration of the sky level. For our analysis, we compute the mean sky level using data at $r > 2.4$ Mpc, making the approximation that the ICL contribution is zero within this region. It is important to assess the extent to which the minimum radius used to estimate the sky impacts our result; varying it between 2.4 and 2.6 Mpc has a negligible impact on the surface brightness profiles or the logarithmic gradients (Section 4.2). The only difference is that when the minimum radius is set to larger values, the statistical uncertainties in the sky level increase due to the decreased area available for sky determination.

The resultant radial profiles for both filters can be seen in Fig. 2. We emphasize that this is the observed profile, with no corrections for cosmological surface brightness dimming, passband (k-corrections), or evolution. Both profiles exhibit a flattening at $r \sim 70$ kpc, demarcating the transition from the BCG to the ICL. After this, the profiles show little structure until $r \sim 1$ Mpc, beyond which they decrease rapidly. To investigate whether the secondary subcluster qualitatively impacts the profile, we also derive the profile using only the upper (Eastern) half of our field of view, which is the region nearest to the subcluster (see Fig. 1). We find that the two profiles are consistent with one another at the radii where the subcluster would be expected to have the greatest contribution to the ICL, indicating that any ICL component centred on this subcluster remains subdominant in our analysis.

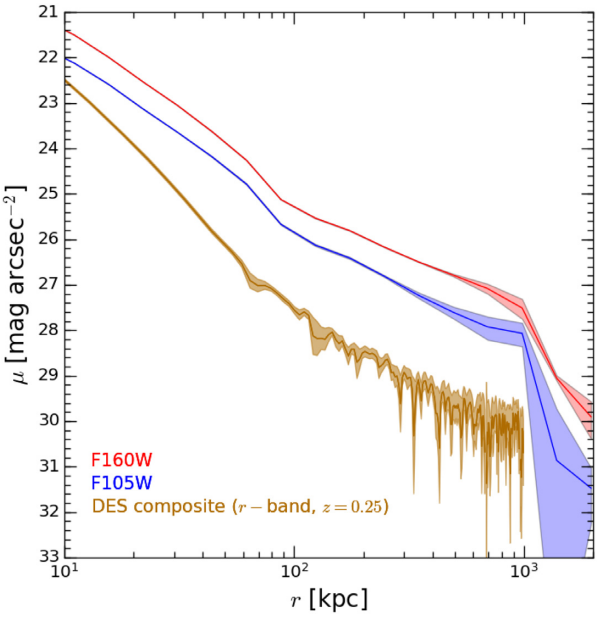

Figure 2. Observed surface brightness profiles for MACS J1149.5+2223 in the $F105W$ (blue) and $F160W$ (red) filters. The profiles shown are as observed, with no evolutionary or passband corrections and no correction for cosmological dimming. Data correspond to the median values within logarithmic bins of width $\Delta\log r = 0.15$. For comparison, we also include the stacked surface brightness profile from Zhang et al. (2019), which is constructed from r-band DES data of ∼300 clusters at $z \approx 0.25$ (brown). While the normalizations differ due to the differences in redshifts and filters, for both the stacked data and MACS J1149.5+2223 a transition from the BCG-dominated to ICL-dominated regime can be seen slightly interior to 100 kpc. Both the MACS J1149.5+2223 and DES data also exhibit a similar profile shape from 100 kpc out to the maximum radii probed by the stacked data.

For comparison, we show the stacked Dark Energy Survey surface brightness profile from Zhang et al. (2019), which is an r-band profile at $z = 0.25$ constructed from an ensemble of ∼300 clusters. The values of the surface brightness are not directly comparable due to the differences in filters and redshift, however, the shapes are. The inner transition from BCG to ICL can be seen in both, although the inner slope is somewhat steeper for the composite than for MACS J1149.5+2223. At larger radii, the profiles appear similar out to the largest radii probed by the DES sample. Beyond this, however, we see evidence for a steepening of the profile.

4.2 Logarithmic gradient

To better quantify the shape, we plot the radial logarithmic gradient of the surface brightness, dlog Σ/dlog r in both bands in Fig. 3, where Σ is the flux per square arcsec.[4] Similar behaviour is evident in both filters; we therefore compute a weighted average of the two data sets,

[3]As a test, we also compute the mean profiles and find consistent results.

[4]The gradient is calculated using the NUMPY gradient function with `edge_order = 2`.

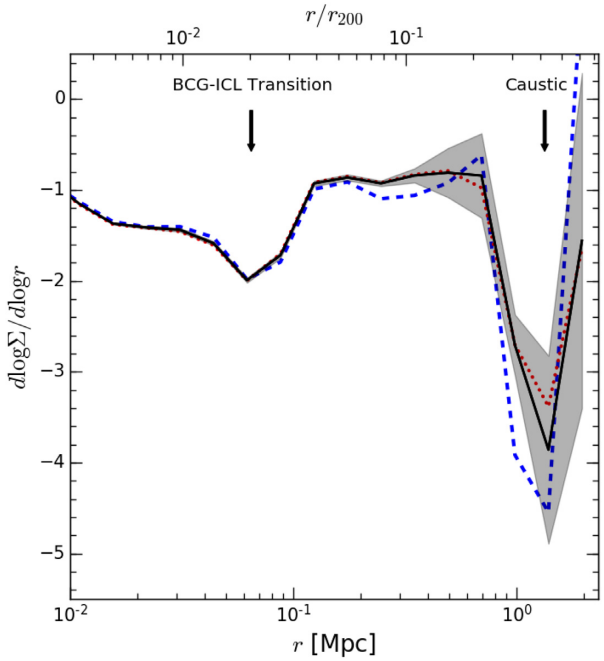

Figure 3. Logarithmic slope of the luminosity surface density. The dashed blue and dotted red curves are for $F105W$ and $F160W$, respectively. The solid black curve is the uncertainty-weighted mean of the two filters, while the grey region corresponds to the 1σ uncertainties. At large radii, the weighted mean and 1σ confidence interval are driven by the $F160W$ data due to the smaller associated surface brightness uncertainties. The transition from the regime dominated by the luminosity of the BCG to that dominated by the ICL corresponds to the inflection at ∼60–70 kpc (∼0.02 r_{200m}). A second, larger dip occurs in the bin centred at 1.4 Mpc (0.44 r_{200m}), which spans radii of 1.2–1.7 Mpc (0.37–0.52 r_{200m}). This dip appears to be a caustic in the density distribution. Based upon the strength of this dip, we interpret this caustic as plausibly corresponding to the splashback radius.

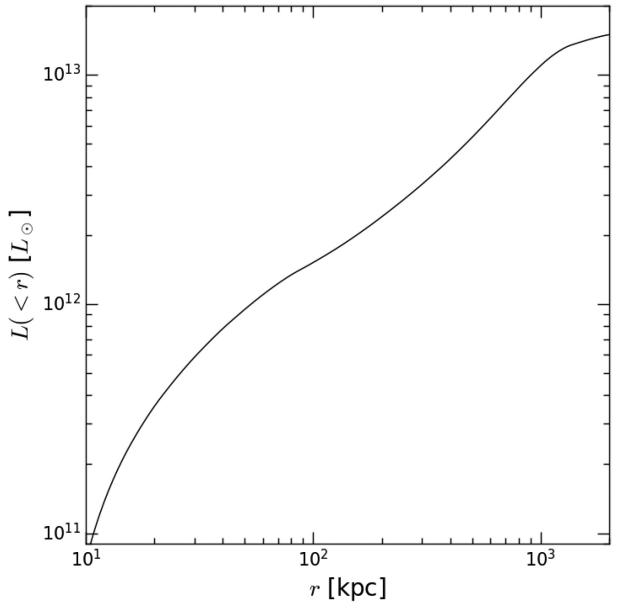

Figure 4. Estimate of the total enclosed luminosity in the BCG + ICL of MACS J1149.5+2223 as a function of radius. This estimate assumes a radially symmetric surface brightness profile. We omit uncertainties since for a merging cluster like MACS J1149.5+2223 this systematic uncertainty will dominate the error budget.

which is shown as the solid black curve and associated uncertainties. Two features are clearly evident. First, the transition from the surface brightness being dominated by the BCG to by the ICL can now be clearly associated with the small dip in the gradient at $r \sim 70$ kpc. Incidentally, this radius is quite similar to the point at which Montes et al. (2021) recently found that the ICL starts to dominate for the nearby cluster Abell 85, and lies within the range expected by the models of Contini & Gu (2021). Second, there is a much stronger feature at $r \sim 1.4$ Mpc. We emphasize that the same feature is seen in both filters, but note that the detection of the upturn in the last radial bin is tentative given the uncertainties. We also verified that a systematic oversubtraction of the sky cannot produce such a feature. On the top axis of Fig. 3, we recast the radius in terms of r_{200m}, as this is useful for facilitating comparison with theoretical predictions. Umetsu et al. (2014) derived a weak lensing mass for this cluster of $M_{200m} = 3.4 \pm 0.7 \times 10^{15}$ $M_\odot$, which corresponds to $r_{200m} = 3.18 \pm 0.22$ Mpc. We use this fiducial value of r_{200m} for the rest of our analysis.

4.3 Total luminosity

We estimate the total enclosed luminosity as a function of radius, interpolating the $F160W$ surface brightness profiles to bins of $d\log r = 0.01$ (Fig. 4). A limitation in this calculation is that we lack full angular coverage and therefore make the approximation of a circularly symmetric surface brightness profile. Given the merging state of MACS J1149.5+2223, this is likely to be a poor approximation. None the less, we find that the total luminosity of the BCG+ICL is $\sim 1.5 \times 10^{13}$ $L_\odot$ within 2 Mpc, indicating that over 90 per cent (50 per cent) of the total observed ICL luminosity lies outside the central 100 kpc (725 kpc). We also find $L \sim 1.3 \times 10^{13}$ $L_\odot$ within 1.4 Mpc (Section 4.2 and Fig. 3), indicating that there is only a modest contribution to the total luminosity beyond this radius.

5 INTERPRETATION OF THE OUTER FEATURE

Recent theoretical work by Deason et al. (2021) predicts the existence of a caustic at the splashback radius (r_{sp}), with $r_{sp} \sim r_{200m}$. Deason et al. (2021) also find secondary caustics at smaller radii for some clusters that experienced significant accretion events in the past. In Fig. 5, we compare our observations with the predictions from Deason et al. (2021) for the logarithmic gradient in the median surface brightness, which are also measured in circular apertures. These predictions come from an ensemble of clusters at $z = 0$ in the C-EAGLE simulations, which span a mass range of $M_{200c} = 10^{14}$ to 2.5×10^{15} $M_\odot$. The theoretical prediction of the curve for each cluster in the ensemble is calculated by taking the median value for a series of angular wedges within each radial annulus. While slightly different than our median calculation, the methods are sufficiently similar that the profiles should be directly comparable. The depth of the feature observed in MACS J1149.5+2223 is consistent with those predicted for the splashback radius. The radius of the observed caustic, which lies in the 0.37–0.52 r_{200m} radial bin (∼0.44r_{200m} bin centre), is smaller than would be expected for the splashback radius in a typical cluster.

There are several possible factors that may explain this difference between the observations and simulations. First, as noted above, secondary caustics do exist for some clusters. We therefore cannot discount the notion that we are viewing a secondary caustic rather

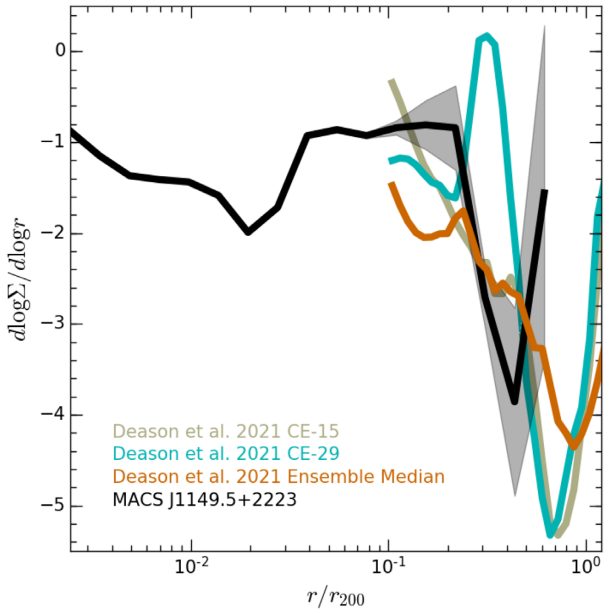

Figure 5. Logarithmic slope of the luminosity surface density as in Fig. 3, but now compared with Deason et al. (2021) profiles from the C-EAGLE simulation. The three curves shown are all derived using the angular median approach of Mansfield et al. (2017). The curve labelled *'Ensemble Median'* is a stack based upon the full sample of 30 simulated clusters. The other two, CE-15 and CE-19, are individual simulated clusters with high accretion rates. The shape and amplitudes of the caustic feature are similar, but the mimima is at smaller radius for MACS J1149.5+2223 than for the simulations.

than the splashback radius. In the simulated clusters published by Deason et al. (2021), however, the secondary caustic dips are typically very shallow (see their figs 2 and 3) and in no instances approach the depth that we see in MACS J1149.5+2223. We therefore consider it unlikely that we are viewing a secondary caustic.

Second, MACS J1149.5+2223 is known to be a complex merging system (Golovich et al. 2016). The ratio r_{sp}/r_{200m} is predicted to be a function of accretion rate, with r_{sp}/r_{200m} decreasing as the accretion rate increases. Because MACS J1149.5+2223 is a merging system, it is expected that this ratio should be less than unity. In Fig. 5, we also include curves for CE-15 and CE-29, which are among the individual simulated clusters with the highest accretion rates. CE-29 is also among the most massive clusters in the simulation ($M_{200m} \sim 3.2 \times 10^{15}$ M$_\odot$), comparable in mass to MACS J1149.5+2223. For these clusters, the splashback radius moves in as far as $\sim 0.7 r_{200m}$. Thus, the dynamical state of the cluster may reduce this discrepancy between the observed splashback radius and simulations. Diemer (2020) find that at even higher accretion rates r_{sp}/r_{200m} converges to 0.65. Given we observe $r_{sp} \simeq 0.37$–$0.52\ r_{200m}$, a high accretion rate for MACS J1149.5+2223 can therefore mostly (but not completely) explain the small observed value of r_{sp}.

Third, it is possible that our estimation of the splashback radius is biased because of our limited azimuthal coverage for this merging system. If there is a local structure that is coherent on the angular scale subtended by our data, then the impact of this structure will persist even with the use of a median profile. If such a structure exists in the bin centred at 1.96 Mpc, then we may be underestimating the splashback radius. Another consequence of the limited azimuthal coverage is the large uncertainty in the last radial bin, as it remains possible (15 per cent probability) that the minimum is at a larger radius.

Fourth, we must consider r_{200m}, which might produce the discrepancy between theory and the observed splashback radius if it is overestimated for our analysis. The r_{200m} uncertainty may be larger than reflected in the statistical uncertainties due to this merging system's ellipticity ($b/a = 0.37$; Umetsu et al. 2018), since we probe along only one direction and complex morphology. The ellipticity is unlikely to be the explanation. Given that our radial profile is offset by only $\sim 27^\circ$ from the major axis of the merger (Umetsu et al. 2018), we are more plausibly underestimating than overestimating r_{200m} along this direction by assuming radial symmetry. Conversely, the complex morphology may provide a partial resolution if M_{200m}, and hence r_{200m}, has been overestimated along the direction of our observations. The mass within the central 1.5 Mpc is, however, sufficiently well determined by multiple groups that this is unlikely to be the full explanation.

The final possibility is that ΛCDM simulations systematically overestimate cluster splashback radii. For example, self-interacting dark matter would decrease the splashback radius (see More et al. 2016, for a discussion of this topic). Published measurements based upon galaxy density and luminosity profiles for various cluster samples, however, yield ensemble values in the range of $r_{sp}/r_{200m} \simeq 0.8$–$1.2$ (More et al. 2016; Chang et al. 2018; Shin et al. 2019; Murata et al. 2020; Bianconi et al. 2021) – all significantly larger than what is observed in this instance.

6 CONCLUSIONS

This paper is the first in a series investigating the properties of the ICL in the HFF cluster MACS J1149.5+2223. We have used the combination of existing data sets and new GO observations to provide contiguous radial coverage from the cluster centre to 2.8 Mpc, which corresponds to $\sim 0.88\ r_{200m}$, in a strip extending south-east from the cluster core. The focus of this paper is the radial surface brightness profile for the cluster, and we also present the methodology employed in our analysis. Our central findings are:

(i) We are able to extract the radial surface brightness profile of the BCG and ICL out to a radius of 2 Mpc, approximately $0.6\ r_{200m}$. This distance is the furthest to which the BCG + ICL profile has been measured for any individual cluster, and is comparable to the distance probed by the stacking analysis of Sampaio-Santos et al. (2021) for 528 DES clusters. The key to reaching these large radii for MACS J1149.5+2223 lies in bridging the gap between the HFF primary and parallel fields to enable a robust sky determination.

(ii) We see a distinct transition in the profile at ∼70 kpc, which we interpret as the radius at which the profile transitions from the BCG to the ICL.

(iii) We identify a sharp steepening of the ICL surface brightness profile beyond 1 Mpc. From the logarithmic derivative of the luminosity density, we find evidence that this transition corresponds to a caustic in the stellar distribution at ∼1.2–1.7 Mpc (approximately 0.37–$0.52\ r_{200m}$). The centre of the radial bin in which the caustic is found is 1.4 Mpc ($0.44\ r_{200m}$).

(iv) Under the assumption of a radially symmetric profile, we calculate that the total luminosity of the BCG + ICL is $\sim 1.5 \times 10^{13} L_\odot$ within 2 Mpc. The luminosity profile indicates that over 90 per cent (50 per cent) of the total BCG + ICL luminosity lies outside of the central 100 (725) kpc.

(v) Recent work by Deason et al. (2021) has argued for the existence of caustics in the ICL at the cluster splashback radius. While those simulations predict that the splashback radius should typically be at $\gtrsim 0.7 r_{200m}$, the strength of the feature in the logarithmic deriva-

tive plot for MACS J1149.5+2223 is consistent with expectations for the splashback signature. If the observed caustic is indeed the splashback radius, the offset relative to the simulations may arise in part from MACS J1149.5+2223's complex dynamics – the splashback radius in a merging system should be smaller relative to r_{200m}.

While this work is the first to detect the ICL beyond 1 Mpc for an individual cluster, similar studies are now possible with minimal additional required data for the remaining HFF clusters. Detections of similar caustics should be achievable in at least some of these systems, and will further shed light on whether these features correspond to splashback radii. Looking forward, upcoming next-generation facilities including *Euclid* and the *Roman Space Telescope* have the potential to enable systematic studies of the extended ICL distribution for large numbers of clusters and galaxy groups out to the splashback radius.

In the shorter term, this paper is the first on the ICL in MACS J1149.5+2223. The partitioning of baryons between the ICL, galaxies, and gas, and the distribution of ICL relative to dark matter will be investigated in subsequent work.

ACKNOWLEDGEMENTS

AHG thanks Yannick Bahe for providing information on the axial ratios of the BCG and ICL in the C-EAGLE simulations. The authors also thank the anonymous referee for thoughtful comments that improved the manuscript. This work is based on observations with the NASA/ESA *Hubble Space Telescope* obtained at the Space Telescope Science Institute, which is operated by the Association of Universities for Research in Astronomy, Incorporated, under NASA contract NAS5-26555. Support for Program number 15308 was provided by NASA through a grant from the Space Telescope Science Institute, which is operated by the Association of Universities for Research in Astronomy, Incorporated, under NASA contract NAS5-26555. The work of TC was carried out at the Jet Propulsion Laboratory, California Institute of Technology, under a contract with NASA.

DATA AVAILABILITY

The data underlying this article will be shared on reasonable request to the corresponding author.

REFERENCES

Adhikari S., Dalal N., Chamberlain R. T., 2014, J. Cosmol. Astropart. Phys., 2014, 019
Adhikari S. et al., 2020, preprint (arXiv:2008.11663)
Alonso Asensio I., Dalla Vecchia C., Bahé Y. M., Barnes D. J., Kay S. T., 2020, MNRAS, 494, 1859
Annunziatella M. et al., 2016, A&A, 585, A160
Bertin E., 2010a, Astrophysics Source Code Library, record ascl:1010.063
Bertin E., 2010b, Astrophysics Source Code Library, record ascl:1010.068
Bertin E., Arnouts S., 1996, A&AS, 117, 393
Bertschinger E., 1985, ApJS, 58, 39
Bianconi M., Buscicchio R., Smith G. P., McGee S. L., Haines C. P., Finoguenov A., Babul A., 2021, ApJ, 911, 136
Borlaff A. et al., 2019, A&A, 621, A133
Brammer G., Pirzkal N., McCullough P., MacKenty J., 2014, Space Telescope WFC Instrument Science Report, Time-varying Excess Earth-glow Backgrounds in the WFC3/IR Channel
Chang C. et al., 2018, ApJ, 864, 83
Contigiani O., Hoekstra H., Bahé Y. M., 2019, MNRAS, 485, 408
Contini E., Gu Q., 2021, ApJ, 915, 106
DeMaio T., Gonzalez A. H., Zabludoff A., Zaritsky D., Bradač M., 2015, MNRAS, 448, 1162
DeMaio T., Gonzalez A. H., Zabludoff A., Zaritsky D., Connor T., Donahue M., Mulchaey J. S., 2018, MNRAS, 474, 3009
DeMaio T. et al., 2020, MNRAS, 491, 3751
Deason A. J. et al., 2021, MNRAS, 500, 4181
Diemer B., 2020, ApJS, 251, 17
Diemer B., Kravtsov A. V., 2014, ApJ, 789, 1
Ebeling H., Edge A. C., Henry J. P., 2001, ApJ, 553, 668
Ebeling H., Barrett E., Donovan D., Ma C.-J., Edge A. C., van Speybroeck L., 2007, ApJ, 661, L33
Fillmore J. A., Goldreich P., 1984, ApJ, 281, 1
Furnell K. E. et al., 2021, MNRAS, 502, 2419
Giallongo E. et al., 2014, ApJ, 781, 24
Golovich N., Dawson W. A., Wittman D., Ogrean G., van Weeren R., Bonafede A., 2016, ApJ, 831, 110
Gonzaga S., Hack W. Fruchter A., Mack J., eds, 2012, The DrizzlePac Handbook. STScI, Baltimore
Gonzalez A. H., Zabludoff A. I., Zaritsky D., 2005, ApJ, 618, 195
Gonzalez A. H., Zaritsky D., Zabludoff A. I., 2007, ApJ, 666, 147
Gonzalez A. H., Sivanandam S., Zabludoff A. I., Zaritsky D., 2013, ApJ, 778, 14
Gunn J. E., Gott J. R. III, 1972, ApJ, 176, 1
Laganá T. F., Martinet N., Durret F., Lima Neto G. B., Maughan B., Zhang Y.-Y., 2013, A&A, 555, A66
Lotz J. M. et al., 2017, ApJ, 837, 97
Mansfield P., Kravtsov A. V., Diemer B., 2017, ApJ, 841, 34
Montes M., 2019, preprint (arXiv:1912.01616)
Montes M., Trujillo I., 2014, ApJ, 794, 137
Montes M., Trujillo I., 2018, MNRAS, 474, 917
Montes M., Trujillo I., 2019, MNRAS, 482, 2838
Montes M., Brough S., Owers M. S., Santucci G., 2021, ApJ, 910, 45
More S., Diemer B., Kravtsov A. V., 2015, ApJ, 810, 36
More S. et al., 2016, ApJ, 825, 39
Morishita T., Abramson L. E., Treu T., Schmidt K. B., Vulcani B., Wang X., 2017, ApJ, 846, 139
Murata R., Sunayama T., Oguri M., More S., Nishizawa A. J., Nishimichi T., Osato K., 2020, PASJ, 72, 64
O'Neil S., Barnes D. J., Vogelsberger M., Diemer B., 2021, MNRAS, 504, 4649
Oemler A., 1973, ApJ, 180, 11
Pirzkal N., 2014, Space Telescope WFC Instrument Science Report, The Near Infrared Sky Background
Planck Collaboration XIII, 2016, A&A, 594, A13
Postman M. et al., 2012, ApJS, 199, 25
Sampaio-Santos H. et al., 2021, MNRAS, 501, 1300
Schombert J. M., 1986, ApJS, 60, 603
Schombert J. M., 1988, ApJ, 328, 475
Science Software Branch at STScI, 2012, Astrophysics Source Code Library, record ascl:1207.011
Shin T. et al., 2019, MNRAS, 487, 2900
Smith R. M., Zavodny M., Rahmer G., Bonati M., 2008, in Dorn D. A., Holland A. D., eds, Proc. SPIE Conf. Ser. Vol. 7021, High Energy, Optical, and Infrared Detectors for Astronomy III. SPIE, Bellingham, p. 70210J
Umetsu K., Diemer B., 2017, ApJ, 836, 231
Umetsu K. et al., 2014, ApJ, 795, 163
Umetsu K. et al., 2018, ApJ, 860, 104
Xhakaj E., Diemer B., Leauthaud A., Wasserman A., Huang S., Luo Y., Adhikari S., Singh S., 2020, MNRAS, 499, 3534
Zhang Y. et al., 2019, ApJ, 874, 165
Zibetti S., White S. D. M., Schneider D. P., Brinkmann J., 2005, MNRAS, 358, 949
Zürcher D., More S., 2019, ApJ, 874, 184
Zwicky F., 1951, PASP, 63, 61

This paper has been typeset from a TEX/LATEX file prepared by the author.